Chapter 9
Nb_3Sn 11 T Dipole for the High Luminosity LHC (CERN)

Bernardo Bordini, Luca Bottura, Arnaud Devred, Lucio Fiscarelli, Mikko Karppinen, Gijs de Rijk, Lucio Rossi, Frédéric Savary, and Gerard Willering

Abstract This chapter describes the design of, and parameters for, the 11 T dipole developed at the European Organization for Nuclear Research (CERN) for the High Luminosity Large Hadron Collider (HL-LHC) project. The results for testing the short models as well as the first 5 m long magnet are also presented. Finally, the production process for the six units, of which four are to be installed in the HL-LHC, is described, with a description of the process for planning the installation. In 2020, these dipoles should be the first Nb_3Sn magnets working in an accelerator.

9.1 Introduction

The Large Hadron Collider (LHC) will undergo a major upgrade to increase the luminosity of proton–proton collisions. The upgrade, called the High Luminosity LHC (HL-LHC or HiLumi LHC) (Apollinari et al. 2017; Brüning and Rossi 2015), calls for a more intense proton beam, with a circulating current of 1.1 A vs. the 0.56 A nominal current value in the LHC. The intensity of the ion beams (usually Pb ions) for ion–ion collisions will actually be increased by a factor of three: from 40×10^9 to 120×10^9 circulating particles. This intensity increase, both for protons and ions, will increase the diffractive losses at the primary collimators, located in LHC Point 7 (P7), which may drive the heat losses in the main dipoles in the dispersion suppressor (DS) region above the quench limit.

B. Bordini · L. Bottura · A. Devred · L. Fiscarelli · M. Karppinen · G. de Rijk · F. Savary · G. Willering
CERN (European Organization for Nuclear Research), Meyrin, Genève, Switzerland
e-mail: Bernardo.Bordini@cern.ch; Luca.Bottura@cern.ch; Arnaud.Devred@cern.ch; Lucio.Fiscarelli@cern.ch; Mikko.Karppinen@cern.ch; Gijs.Derijk@cern.ch; Frederic.Savary@cern.ch; Gerard.Willering@cern.ch

L. Rossi (✉)
CERN (European Organization for Nuclear Research), Meyrin, Genève, Switzerland

University of Milan, Physics Department, Milano, Italy
e-mail: Lucio.Rossi@cern.ch

D. Schoerling, A. V. Zlobin (eds.), *Nb_3Sn Accelerator Magnets*, Particle Acceleration and Detection, https://doi.org/10.1007/978-3-030-16118-7_9

To avoid limiting the machine due to this effect, various countermeasures have been studied, and the solution chosen was to intercept these diffractive losses via warm absorbers (also called *collimators*) placed in the cold region of the LHC. The most elegant and practical way to introduce a room-temperature zone in the DS, at a location corresponding to the middle of the second dipole of the DS cell, was to substitute an LHC dipole (8.33 T of central field and 14.3 m of magnetic length) with a magnet of 11 T with a length of approximately 11 m, yielding the same bending strength while saving about 3.5 m. The 11 T field in the magnet bore inevitably calls for Nb_3Sn technology. The space gained, thanks to the higher field and shorter length, is sufficient to insert a cold–warm–cold bypass on which to allocate all lines for cryogenic and electrical continuity of the circuits in series in the LHC arc, and the target collimator long dispersion suppressor (TCLD). For reasons of beam dynamics (reduction of the orbit excursion with respect to the ideal trajectory) and to reduce the technology risk associated with the innovative and relatively expensive Nb_3Sn superconductor, we decided to split the 11 T dipole into two magnets of 5.5 m length, with the bypass and collimator in the middle. A schematic layout of the assembly with its position in the LHC is shown in Fig. 9.1.

9.1.1 History of the 11 T Project

The possibility of using 11 T dipoles in the LHC was first envisaged at the LHC Performance Workshop in January 2010 (Carli 2010, 29). After a preliminary study (de Rijk et al. 2010), it was included in the HL-LHC project and in the main goals of the European Organization for Nuclear Research (CERN) High-Field Magnet (HFM) program (Bottura et al. 2012). The project was set up after the end of 2010 as a close collaboration between CERN and the Fermi National Accelerator Laboratory (FNAL). FNAL has carried out an extensive research and development (R&D) program on dipoles for reaching 10–11 T for the Very Large Hadron Collider (VLHC) (see also Chap. 7, Cos-theta Nb_3Sn Dipole), besides participating in the US LHC Accelerator Research Program (LARP) (Zlobin 2010). This was in a period when CERN was restarting Nb_3Sn R&D, with a main focus on the Inner Triplet program for the HL-LHC.

A parallel program was established, with two companion lines: one in FNAL and another in CERN, as described in detail in Chap. 8, The Nb_3Sn 11 T Dipole for the High Luminosity LHC (FNAL). The initial scope was to design and manufacture short models and one 5.5 m long prototype in each laboratory, allowing for small differences in design. In this program, intensive technology transfer from FNAL to CERN took place, especially in the domain of Nb_3Sn coil technology.

During its course the plan was modified, mainly because the funding profile at FNAL was reduced and shortened, so FNAL concentrated on the design, construction, and test of a few short models, initially with a length of 2 m, and then 1 m.

A detailed description of the design, and the similarities and differences between the FNAL and CERN designs, as well as the initial R&D, can be found in Chap. 8,

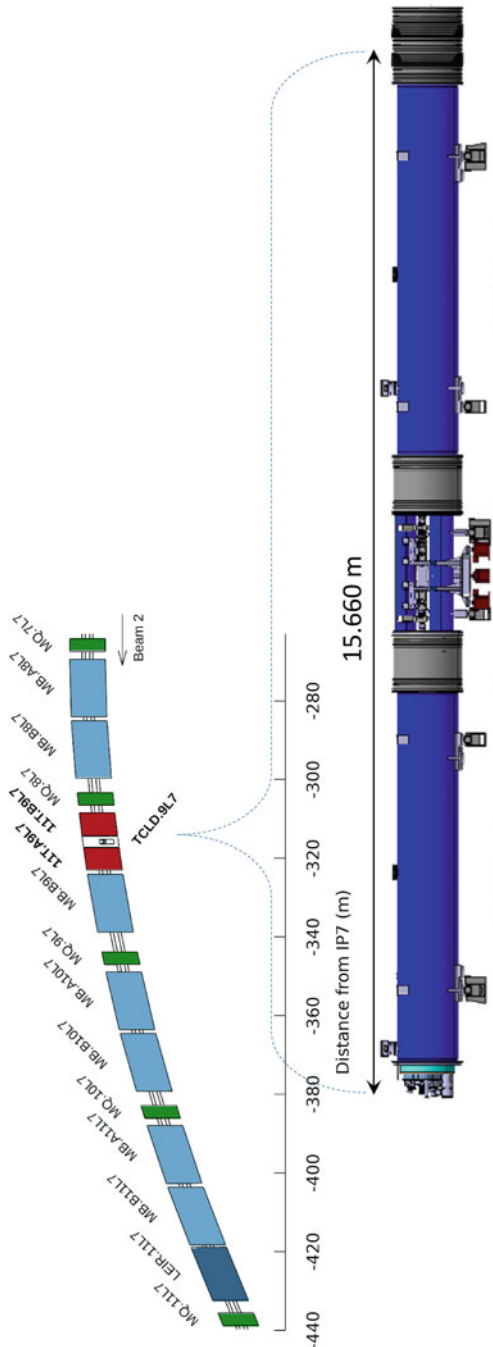

Fig. 9.1 Schematic of the 11 T cryo-assembly, with the bypass hosting the collimator at the center. In the dispersion suppressor (DS) cells (the array in the top where LHC dipoles are in light blue) one standard dipole is replaced by the 11 T cryo-assembly, indicated in red

The Nb_3Sn 11 T Dipole for the High Luminosity LHC (FNAL), and are not discussed here. In this chapter we concentrate on the specifics of the R&D at CERN, on the design's main features, as well as short model testing, both single and two-in-one apertures, and on the industrialization aspects related to long magnet production for the HL-LHC.

9.1.2 Present Scope of the 11 T Project

It is foreseen that most of the HL-LHC installation work, including the Nb_3Sn Inner Triplet quadrupoles, will take place during the period 2024–2026, known as Long Shutdown 3 (LS3). The LHC Injectors Upgrade (LIU) project, which will allow the production of more intense beams for the LHC (Damerau et al. 2014), will, however, already have been carried out during the period 2019–2020, known as Long Shutdown 2 (LS2). It is then foreseen that ion beams will be collided at their maximum intensity during LHC Run 3 (2021–2023), i.e., after LS2. In the same period, HL-LHC high-intensity proton beams will also be tested. For this reason, the diffractive losses in P7 described above could play a limiting role in LHC Run 3.

To avoid this limitation, it was decided in 2010 to prepare the 11 T dipole with its collimation system for installation during LS2, requiring that both 11 T magnet assemblies (one per side with respect to LHC P7) and their ancillary systems are ready by 2019. Originally, it was foreseen that further sets of 11 T dipoles would be installed in LS3: an additional set in both sides of the P7 DS and around the Point 2 (P2) interaction point (Alice detectors), for a total of 16 11 T dipoles, each 5.55 m in length. Because of a re-evaluation of heat deposition (in particular in P7), and because other solutions could be devised with modified beam optics, it was later decided that these additional 11 T dipoles would no longer be necessary. They have been removed from the HL-LHC baseline, which is hence presently limited to four 11 T dipoles, to be installed in two sets around Point 7 at LHC locations MB.AR7 and MB.AL7.

9.2 Magnet Design

9.2.1 Design Constraints

The main constraint is due to the fact that the 11 T dipole pair is a part of the LHC main circuit and, as such, is powered in series with the other 153 LHC two-in-one-aperture dipoles comprising one of the eight LHC main dipole circuits. Each 11 T dipole pair must have an integrated transfer function (ITF) as near as possible to that of the LHC main dipoles over the whole dynamic range, from the injection energy of 0.45 TeV (7.7 Tm of bending strength) to the collision energy of 7 TeV (119.2 Tm of bending strength). These values for the bending strength must be obtained at the

nominal current of the main bending (MB) circuit, i.e., 760 A at the 0.45 TeV injection energy and 11.85 kA at the 7 TeV collision energy. A second condition was to respect the LHC's basic geometry: the distance between the center of the two apertures (194 mm at 1.9 K) and the position of the cryogenic and electrical lines passing through the yoke. Finally, the timescale did not allow for a long period of R&D. It was therefore decided to rely on a design concept as close as possible to that of the LHC MB dipoles, from which CERN has accumulated more than two decades of experience (Rossi 2004): the two-layer cos-theta coil layout, with the force supported by a classical collar structure, a vertically split iron yoke, and an external shrinking cylinder also serving as a helium vessel. Thanks to CERN's experience and to the FNAL program on the Nb_3Sn cos-theta layout with collars, the initial decision on the layout was taken.

The preliminary design study proved that all main design criteria, i.e., field strength with a reasonable ITF over all of the dynamic range, critical current margin, and field quality (both at injection and at high field), could be met with the available Nb_3Sn wire properties, despite the considerable difficulties given by the various constraints. Structural and protection issues were left to a more detailed, realistic design.

9.2.2 Basic Features

Different from the LHC MB, the 11 T dipoles have separate stainless-steel collars for each aperture, compared to common stainless-steel collars in the case of the LHC MBs. This design change was introduced to allow a better-controlled symmetric loading of the coils and make it possible to test the collared coils in a one-in-one configuration without the need for de-collaring prior to integration in the two-in-one cold mass. To make maximum use of the existing infrastructure and cold-mass assembly tooling, the outer contour of the cold mass was chosen to be identical to the LHC MBs. The location and the section of the slots' bus-bars was to be preserved, as well as the location of the heat exchanger in the iron yoke.

A nominal field of 11 T requires a magnet that is about 11 m long. To reduce the risks associated with the fabrication of brittle Nb_3Sn coils, the original 11 m long magnet was split into two units, each 5.5 m long and with straight coils, not bent as in the MBs. The sagitta of the beam trajectory in each 5.5 m long straight magnet is only around 2 mm compared to 9 mm in a standard MB. During the initial phase of the project, it was considered important to compensate for the effect of the sagitta on the free aperture by enlarging the coil aperture to 60 mm (this is 56 mm in the LHC dipoles). Later, it was decided to use existing spare beam screens from the LHC without an increased free aperture.

The field quality targets were similar to those of the LHC MB, and at the 10^{-4} level at the reference radius of 17 mm, and special attention was to be paid to the multipoles arising from persistent currents induced in the inherently larger filaments

of the available Nb_3Sn strands and the higher yoke saturation (with a larger magnetic flux conveyed in the same yoke as the MB).

A further important advantage of this solution is the possibility of placing the collimator between the two 5.5 m 11 T dipoles, reducing the orbit excursion, as mentioned above.

To ensure reliable operation, the design goal was to provide an operational margin of 20% on the load line, as for other Nb_3Sn HL-LHC magnets.

The initial design of the 11 T dipole is described by Karppinen et al. (2012) and Zlobin et al. (2012).

9.2.3 Conductor Choice and Nominal Dimensions

The parameters of the strands and the Rutherford cable were selected based on the required number of ampere-turns to generate the requested ITF under the 20% operating margin, the available coil space, and the maximum number of strands possible in the cabling machine. For this last constraint, the most stringent limits were between CERN (40 strands), and FNAL (42 strands). The selected strand diameter was 0.7 mm, with an expected cable thickness in the range 1.2–1.3 mm (depending on the allowed compaction). The strand geometry and performance specification are summarized in Table 9.1.

The optimization of cable parameters was done jointly by FNAL and CERN (Zlobin et al. 2012), and included the selection of the cable cross-section geometry and compaction to achieve good mechanical stability of the cable and acceptable I_c degradation (less than 10%), incorporating a stainless-steel core (25 μm thickness), and preserving a high residual resistivity ratio (RRR) of the Cu matrix (RRR larger than 100 in extracted strands).

Various strand designs, with different technologies (Restack Rod Process® (RRP) and PIT), sub-element number, size, and distribution in the cross-section were considered for the optimization. Trial cabling runs at FNAL in the R&D phase were done using Nb_3Sn wires produced using the Restack Rod Process® by Oxford Superconducting Technologies (OST) (see Chap. 8, The Nb_3Sn 11 T Dipole for the High Luminosity LHC (FNAL)). The architectures considered were baseline RRP108/127, as well as alternative layouts, mainly the RRP150/169 and RRP132/

Table 9.1 Nb_3Sn wire geometry and specifications

Description	Value
Strand diameter (mm)	0.70
J_c (12 T, 4.2 K) (kA/mm^2)	>2.45
Effective filament size D_{eff} (μm)	<41
Twist pitch (mm)	14
Cu RRR (virgin state)	>150
Cu fraction (%)	53.5 (±2)

RRR residual resistivity ratio

Table 9.2 Cable geometrical parameters

Parameter	Un-reacted	Reacted
Mid-thickness (mm)	1.25	1.30
Thin edge (mm)	1.15	1.19
Thick edge (mm)	1.35	1.40
Width (mm)	14.70	15.08
Keystone angle (°)	0.79	0.81

169 layouts, including a low RRR RRP108/127. A cable baseline was generated, with the parameters reported in Table 9.2.

Cabling trials at CERN considered both OST-RRP strands, as well as powder-in-tube (PIT) wires from Bruker European Advanced Superconductors (B-EAS). Most of this work was based on two architectures: PIT 114 and PIT 120. A direct result of this R&D was the observation that PIT is much more sensitive to cable compaction than RRP. The baseline cable geometry resulted in an average degradation of 6%, with cases largely in excess of the 10% acceptance limit. To remain compatible with PIT it was found necessary to reduce the keystone angle from the baseline 0.79° to the range 0.4–0.5°. This corresponds to an increase of the cable's thin edge by 40 μm, which was found to reduce both J_c and RRR degradation due to cabling. It should be noted that this change could not be absorbed in the rather strict cross-section, and would require an iteration of the magnetic design.

At this stage of the project a decision on baseline strand and cable geometry was taken, based on the following observations.

- PIT technology at this geometry (small strands) and field level (12 T) has a critical current density up to 20% lower than that of RRP wires (below specification), is more sensitive to cabling compaction, and has a higher cost. While in the initial stage of the project the volume of magnets was sufficient to justify this alternative route, following re-scoping in 2016 the PIT variant was discarded.
- Among the various RRP architectures, the 132/169 and 150/169 layouts have the advantage of a smaller filament size, which is of importance to reduce persistent current effects. The 108/127 layout, on the other hand, had a lower cost owing to better industrial production maturity. For this reason the RRP108/127 was taken as reference, and the alternative RRP strands were discarded.

The final geometrical parameters and performance considered for the magnet design are, then, those reported in Table 9.1 (strand) and Table 9.2 (cable). During the reaction, Nb_3Sn strands expand due to the phase transformation (Andreev et al. 2002). The parameters of the cable cross-section are presented for un-reacted and reacted cables. The geometrical parameters for the coil winding and curing tooling were determined from the un-reacted cable cross-section, whereas the geometrical parameters for the coil reaction and impregnation tooling were based on the reacted cable dimensions. The latter were also used for the magnet electromagnetic and structural optimization.

Cable samples for qualification and model winding, with rectangular and keystoned cross-sections, with and without a stainless-steel core, were fabricated and initially tested at FNAL, and later also at CERN. Based on the experimental data, the measured I_c degradation from cabling after optimization was less than 4%.

9.2.4 Magnetic Design

The main electromagnetic design challenges of the two-in-one-aperture 11 T dipole are to match the MB ITF, to control the magnetic cross-talk between apertures, and to minimize the magnitude and variation of non-allowed multipoles (Auchmann et al. 2012).

The coil cross-section was optimized using the reacted cable parameters and a 100 μm insulation layer around the cable. The early-stage preliminary design used the iron yoke shown in Fig. 9.2a, leaving a radial space of about 30 mm for the collars. The optimal configuration, delivering 11.21 T at 11.85 kA in a two-in-one configuration, was found with a six-block layout of 56 turns with 22 turns in the inner layer and 34 turns in the outer layer, as shown in Fig. 9.2b.

The coil ends were optimized first to find the optimal mechanical configuration based on easy- and hard-way strain in the cable, as well as the amount of torsion over the unit length. The lead-end optimization also included the layer jump and the transitions between the winding blocks. The relative axial positions of the end blocks were then optimized to minimize the integrated harmonics.

It was decided to use this coil design for the short models and then, before scaling up to the full length, re-optimize the coil cross-section with the experimental data from the magnetic measurements of the short model magnets along with the feed-back from coil fabrication.

The nature of the magnetic flux pattern in the two-in-one yoke configuration requires additional features to minimize the cross-talk between the apertures, in particular for the b_2 component. The two holes in the yoke insert reduce the b_2 variation from 16 units to 13 units. Such large cross-talk indicates that the distance between the apertures and the overall size of the yoke would need to be increased for such a high field magnet. The magnetic design was optimized for the two-in-one configuration for the accelerator. Most models were assembled and tested as a single aperture structure, without any attempt to adjust the field quality for such a configuration.

In dipole magnets the iron saturation typically gives rise to a variation of the b_3 and b_5 components. The shape of the cut-out on top of the aperture was optimized to reduce the b_3 variation by 4.7 units when compared to a circular shape. In addition to the holes in the yoke insert, an array of three smaller holes and the position of the hole for the tie-rods were used to further reduce the b_3 variation by 2.4 units, such that the iron saturation induced a variation in b_3 and b_5 of 0.51 and 0.35 units, respectively, between injection and nominal current.

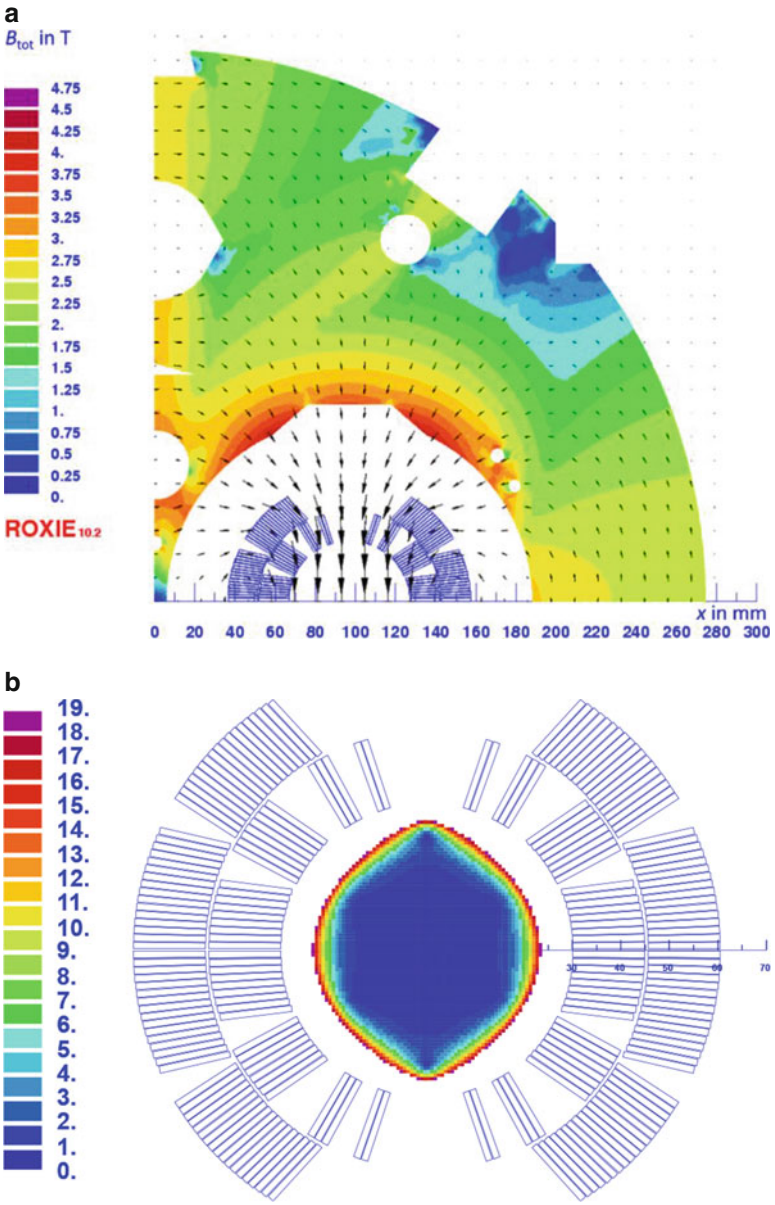

Fig. 9.2 (**a**) Two-in-one model used for coil optimization; (**b**) coil cross-section, with relative field errors in units

Due to the stronger iron saturation effect, the Nb_3Sn dipoles will be stronger than the MB at intermediate excitation levels, the peak difference being 2.4 Tm at 6.7 kA. This difference can be compensated with the foreseen 250 A bi-polar trim power converters to be installed across the 11 T dipoles.

Owing to the larger filament size in Nb_3Sn strands when compared to Nb-Ti strands, the scaled b_3 component due to the persistent currents in the 11 T dipole is about 44 units at the LHC injection current. The magnetization effect strongly depends on the current pre-cycle and the lowest current reached during the cycle, the so-called reset current $I_{res.}$ Using $I_{res} = 100$ A the sextupole component can be reduced to stay within ± 20 units between I_{inj} and I_{nom}, which is acceptable for the LHC (Holzer 2014). In addition, as shown by the measurements quoted below, flux jumps strongly affect the filament magnetization below 1 T and reduce the projected b_3 effect, which is a beneficial effect at the expense of reproducibility.

9.2.5 Mechanical Design

The goal of the mechanical design is to provide a rigid clamping of the superconducting coil with minimum distortion of the conductor positioning, whilst maintaining at all times the stresses at an acceptable level for the fragile Nb_3Sn. A detailed structural analysis was carried out to explore the optimal parameter space for the magnet assembly.

The design concept for the magnet was inspired by the 1 m long LHC MBFISC model magnet (Ahlbäck et al. 1994), and the collar thickness was chosen for maximum rigidity in the available space to minimize the spring-back effect after the collaring process.

The Nb_3Sn cos-theta accelerator magnets developed at FNAL typically feature the pole being heat-treated and potted in the coil. For a quadrupole it is still possible to apply some pre-stress at the pole through the mid-plane, but for a dipole the angular difference between the pole turns and the mid-plane makes this much more complicated. It either requires deforming the coil elliptically in the mid-plane or applying a uniform radial pressure on the coil's outer surface. The first, most commonly applied, method requires a very delicate balance between overloading the mid-plane turns and not unloading the pole turns at full field. For this reason, an integrated pole is not optimal for a collared dipole structure. To overcome such a shortcoming a new concept based on a removable pole was developed for this project (Karppinen et al. 2012). It allows well-controlled adjustment of the coil pre-compression at the poles without overloading the mid-plane. An additional Cu-alloy filler wedge, which is potted together with the coil, is added to the outer layer to match the azimuthal size of the inner layers to simplify the pole wedge geometry as shown in Fig. 9.3. To protect the fragile Nb_3Sn coils during the collaring process, 2 mm thick stainless-steel loading plates are added at the pole, and a separate impregnation pole provides the accurate size for the pole region of the impregnated coil.

In the collared coil the stress pattern can be tuned by varying the thickness of the shims at the pole. The pole shim opens the possibility of achieving an optimal stress distribution when the magnet is powered by limiting the mid-plane stress while keeping the poles under compression. The separate pole wedge reduces the peak

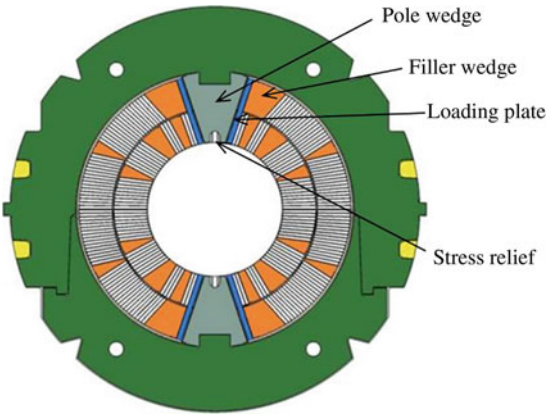

Fig. 9.3 The collared coil concept for the CERN magnet bending, 11 T dipole (MBH)

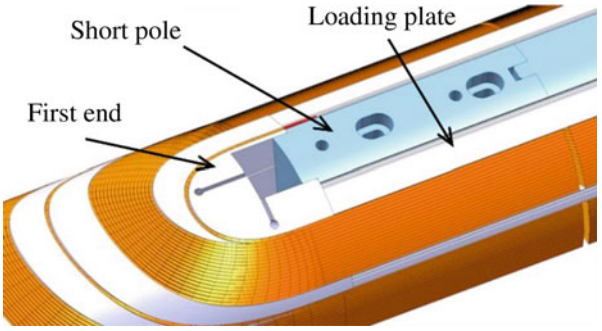

Fig. 9.4 Coil return end showing transition region

stress around the stress-relieving notch by a factor of two as compared to collars comprising the pole area. This reduction is achieved by having every second pole collar carry the load, interleaved with "filler collars" that have a slight clearance from the coil. During the development phase it is also possible to use a shim between the pole wedge and the collar nose to fine-tune the coil pre-stress without taking the coil assembly apart.

The thickness of the collar nose shim is reduced from 0.2 mm in the straight part to 0.1 mm over 55 mm towards the ends, thus linearly reducing the coil stress. This measure has been taken to avoid a discontinuous stress pattern in this delicate area, minimizing any shear stress in the reacted Nb_3Sn coils. The first end spacer has a longitudinal slit to make it more flexible. The other end spacers feature swivel joints in the spacer legs (not shown in Fig. 9.4) to minimize the risk of insulation damage during the fabrication process. Resin-rich volumes, which may have compromised the structural integrity of the coils, have been excluded.

Stainless-steel end saddles are used during the reaction, but they are then replaced with five-axis-machined epoxy-glass (EPGC 3) saddles prior to impregnation, which better matches the transverse rigidity of the coil and reduces the risk of damaging the

Table 9.3 Maximum azimuthal coil pre-stress in pole and mid-plane regions

	Azimuthal coil stress (MPa)				
Position in coil	Under press	Collared coil	Cold mass	Cool-down	$B = 12$ T (min/max)
Inner pole	−126	−92	−143	−115	−27/−5
Outer pole	−87	−52	−65	−61	−37/−5
Inner mid-plane	−115	−55	−65	−58	−134
Outer mid-plane	−91	−66	−95	−94	−127

leads coming out in the mid-plane. They also eliminate the risk of electrical insulation defects in this region.

The wedges separating the winding blocks are usually made of Cu or Cu-alloys. Wedges made from such materials would lose mechanical strength during the coil reaction process. New wedges were developed in collaboration with industry using oxide dispersion strengthened (ODS) Cu-alloy, which retains superior mechanical properties (elastic limit over 240 MPa) after the reaction, and hence minimizes the distortion of the coil geometry due to plastic deformation under stress during assembly and operation. ODS is also thermally and electrically very similar to the "traditional" Cu-alloys.

The collared coils are assembled between the yoke halves and the central yoke insert, and the two 15 mm thick stainless-steel outer shells. The shells are welded together in a welding press to form the shrinking cylinder. During this operation a tensile stress of about 300 MPa is developed in the shrinking cylinder. The yoke inner radius is 0.115 mm larger than the collar outer radius, and there is a horizontal offset of 0.135 mm between the centers of the yoke and the collar radii. This offset increases the radial interference between the somewhat deformed collared coil assembly and the yoke by 0.020 mm, thus minimizing the elliptical deformation of the coils. The reduction in elliptical deformation reduces the sensitivity for assembly tolerances and improves the field quality. This interference is also important for maintaining contact between the yoke and the collared coil at the operating temperature. The yoke gap is closed at room temperature and remains closed up to 12 T field in the bore. Table 9.3 lists the evolution of the coil stress during the fabrication process, at the operating temperature, and during excitation. The poles remain under compression at all times, and the maximum coil stress is less than 145 MPa.

9.3 11 T Dipole Development at CERN

The joint 11 T dipole R&D program at CERN started in 2011 with transfer of the technology developed at FNAL, and with adjustments to the LHC MB specific design features (Savary et al. 2015). At CERN, development was undertaken having in mind the technology suitable for scaling up to the long magnets for installation in the accelerators. In parallel to the R&D, the large tooling for the manufacture of the

long magnets was designed, procured, and installed in the CERN Large Magnet Facility.

9.3.1 CERN Model Design and Fabrication Procedure

Twenty-three 2 m long coils were fabricated during 2013–2018, and assembled in seven single-aperture and two double-aperture short models. The main variants explored are given in Table 9.4, including the strand type, the impregnation procedure followed, and the use of the coil. The details of the model design and fabrication procedures are presented in this subsection.

9.3.1.1 Conductor for the R&D Phase and for Series Production

For the R&D phase CERN has procured nearly 400 km of 0.7 mm diameter Nb_3Sn wire of various layouts. Following successful model results, to cover the series construction phase, an additional 1100 km of Nb_3Sn wire of the 108/127 layout are under procurement according to the specifications reported in Table 9.2. About 800 km out of the 1100 km have already been delivered and fully qualified. Table 9.5 gives a summary of the R&D and production conductors in terms of cable unit lengths produced or under procurement and production.

Overall, only a few billets are below I_c specification, but still above 95% of the specified critical current value of 440 A at 12 T and 4.22 K. The baseline cable

Table 9.4 CERN conductors and coil parameters

Coil	Strand type	Impregnation S/P[a]–A/B[b]	Comment
101, 102	Copper	S–A	Practice coil
103	WST[c]	S–A	Practice coil
104	RRP54/61	S–A	Practice coil
105, 106, 107	RRP108/127	S–A	
108, 109	RRP132/169	S–A	
110	RRP132/169	P–B	Practice coil
111, 112, 113	RRP132/169	S–B	
114, 115	RRP150/169	P–B	
116, 117	RRP150/169	P–B	
118	RRP108/127	P–B	Practice coil
119, 120, 121, 122, 123	RRP108/127	P–B	

[a]"S" stands for gelling and curing under vacuum; "P" stands for gelling and curing under pressure, typically 3–3.5 bar

[b]"A" stands for single resin entry point for impregnation; "B" stands for uniformly distributed injection channels along the coil in the mid-plane

[c]Western Superconducting Technologies Company, Ltd. (WST), China

Table 9.5 Summary of all unit lengths of 0.7 mm Nb_3Sn cables, by different type or layout, produced for the 11 T project by CERN

Wire layout	Unit lengths produced	Cable length (m)	Coil
WST (Nb_3Sn low grade)	2	235	Model
RRP54/61 (low RRR)	1	235	Model
RRP108/127 (low RRR)	4	235	Model
RRP169	10	235	Model
PIT114 or PIT120	6	235	Model
RRP108/127, RRP132/169 (low grade)	2	655	Long dummy
RRP169	3	655	Prototype
Final RRP108/127	2	655	Prototype
Final RRP108/127	19 out of 30	655	Series

produced at CERN has an average J_c degradation of 2% with a maximum of 5% for the RRP strands.

The RRR >150 specification for virgin wire has been respected during production, and the RRR is also larger than 100 after a 15% deformation reduction (rolling), which is representative of the deformation undergone by the strand during the cabling process (note that this last test is not a contractual obligation). It is important to remark that, despite strong initial concerns because of the relatively small wire diameter for such a large current density, the large-scale production of Nb_3Sn for the 11 T dipole is turning out to be a great success.

9.3.1.2 Insulation

Despite the tight schedule of the project, a considerable effort was made at CERN to introduce some innovative technology into coil fabrication.

The first example is the re-introduction of mica in the cable insulation, as illustrated in Fig. 9.5. Similar mica-based insulation was used in the early stages of R&D for the KEK race-track (see Chap. 3, Nb_3Sn Accelerator Magnets: The Early Days (1960s–1980s), and then for the CERN-Elin (see Chap. 4, CERN–ELIN Nb_3Sn Dipole Model) and University of Twente/CERN (see Chap. 5, The UT-CERN Cos-theta LHC-type Nb_3Sn Dipole Magnet) Nb_3Sn dipole projects in the 1980s and 1990s, but this was not pursued further in later realizations.

The insulation of the cables used in CERN models (until SP106), and the first prototype, is made of a 25 mm wide, 0.08 mm thick mica tape shaped around the cable, with a 0.07 mm thick layer of S2-glass braided over the mica layer. The mica layer provides a continuous and solid dielectric barrier around the cable, while the S2-glass layer braided over the mica layer provides an additional turn separation and gluing after impregnation with epoxy. Room-temperature tests confirmed the excellent electrical properties of this insulation. The cable insulation thickness at

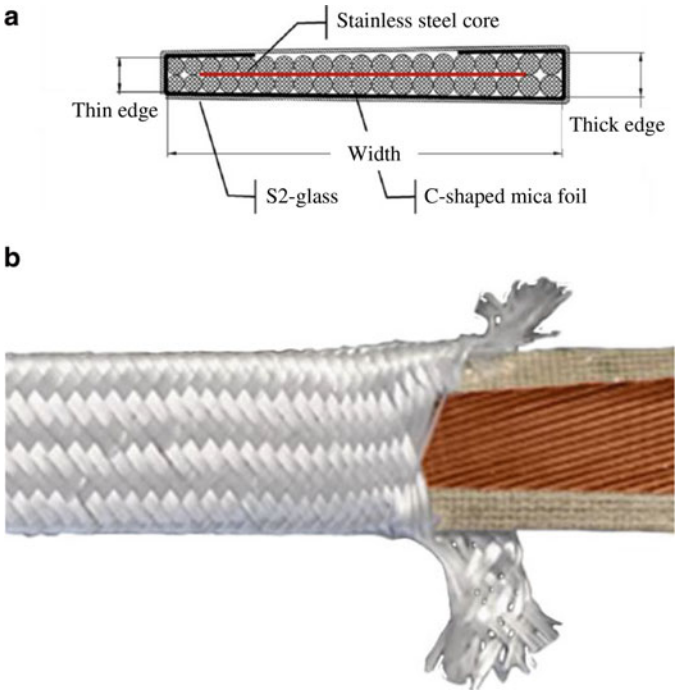

Fig. 9.5 Cable insulation based on S2-glass braided on mica tape (CERN insulation): (**a**) schematic; and (**b**) photograph

production is 0.15 mm. It is reduced to about 0.11–0.14 mm when compressed at about 30 MPa.

The mica tape (see Fig. 9.5) is folded over the cable and covered by a layer of S2-glass braided through a continuous process. At the beginning there was much concern about the possibility that the mica layer would have been a barrier to easy penetration of the resin inside the Rutherford cable. Experience proved that it was not an issue. To facilitate resin flow inside the cable, the mica layer only wraps the two smaller edges and one wide face of the cable, and was designed to cover only about 40% of the other wide face. The layout turned out to be non-optimal for stress distribution over the cable and has recently been modified, see Sect. 9.3.4 below.

9.3.1.3 Coil Technology

The two layers of the coil are wound from one cable unit length without an interlayer splice. In addition to the re-introduction of mica, these are the main technological innovations from CERN R&D:

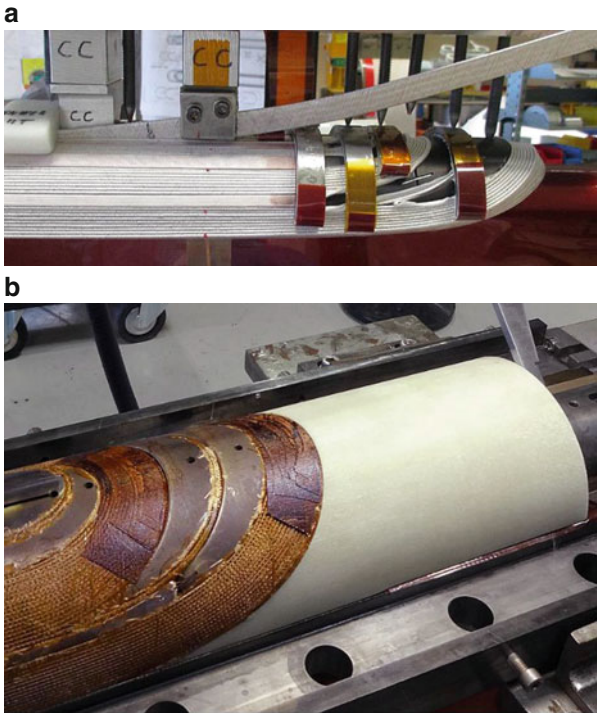

Fig. 9.6 (**a**) Inner-layer lead end with flexible-leg spacers and stainless-steel technology saddle; and (**b**) reacted coil equipped with EPGC22 saddle before impregnation

1. Wedges made from high-performance copper alloy, DISCUP C3/30 ODS copper. ODS wedges minimize coil plastic deformation, while having the elastic, electrical, and thermal properties of Cu even after the heat treatment.
2. Coil end spacers made of AISI 316 L stainless steel, manufactured by using the selective laser sintering process, which provides a short turnaround time if shape modifications are required.
3. Coil ends, some with longitudinal slits and others with swivel joints in the spacer legs. Besides avoiding the resin not reaching the required zone and possible damage to the insulation, it also facilitates winding accuracy, as shown in Fig. 9.6a.
4. Replacement of the metallic end saddle with EPGC-22 non-metallic material.

The first coils were fabricated using the same process and tooling design that was developed at FNAL (see Chap. 8, The Nb_3Sn 11 T Dipole for the High Luminosity LHC (FNAL)). Modifications were then introduced to address the specific features of the CERN coil design. Coil winding mostly follows the process set up at FNAL, with ceramic binder (ceramic matrix CTD-1202-X) but cured to the nominal cross-section. The coil is reacted in a reaction fixture using a three-step cycle, similar to HT1 used at FNAL: 210 °C for 48 h, 400 °C for 48 h, and finally 640 °C for 50 h in an argon atmosphere.

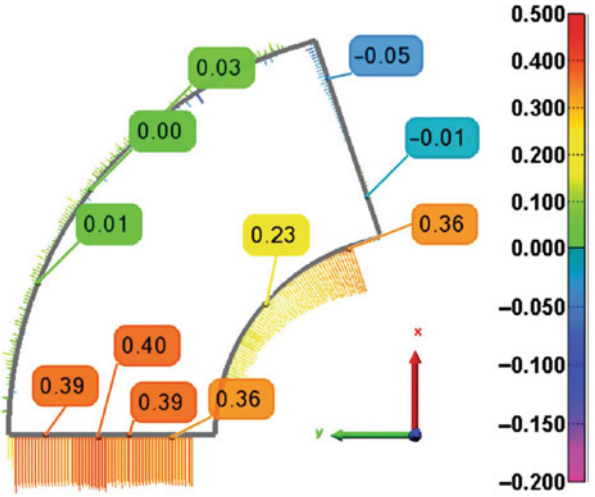

Fig. 9.7 Coil 105 size measurements

After reaction, the coil is transferred into the impregnation mold, the coil leads are spliced to flexible Nb-Ti cables, and the metallic end saddles are replaced by the non-metallic saddles. The usual FNAL flushing, thermal treatment, and final impregnation with CTD-101K epoxy is carried out.

The impregnated coils are measured with a portable 3D measurement arm every 15 cm along the coil, without applying pressure. Each set of measured points in each cross-section is fitted to the CAD model to define the deviations from the nominal sizes. The outer diameter and the loading plate are used as datum surfaces. An example of the measurement data is shown in Fig. 9.7. The variations for the coil outer radius and the pole surface from the design values are small, less than 0.05 mm. The coil mid-plane position is off by 0.4 mm (compared with 0.1 mm in FNAL coils). The deviation of the inner radius is also quite large, ~0.4 mm, but this is not an important parameter for magnet assembly. The measurements also show a considerable longitudinal variation (sometimes called waviness), typically ±0.2 mm, i.e., three to four times that for Nb-Ti. The issue related to the coil size is discussed below (see Sect. 9.3.4).

9.3.1.4 Ground Insulation and Quench Protection Heaters

Robust ground insulation around the coils consists of four layers of 0.125 mm thick polyimide film, which provide the required dielectric strength of 5 kV at room temperature.

The quench protection heaters are large, flexible copper-coated austenitic steel strips glued onto a 0.050 mm thick polyimide film that withstands high voltages, low temperatures, high compression forces, and ionizing radiation. The 0.025 mm thick

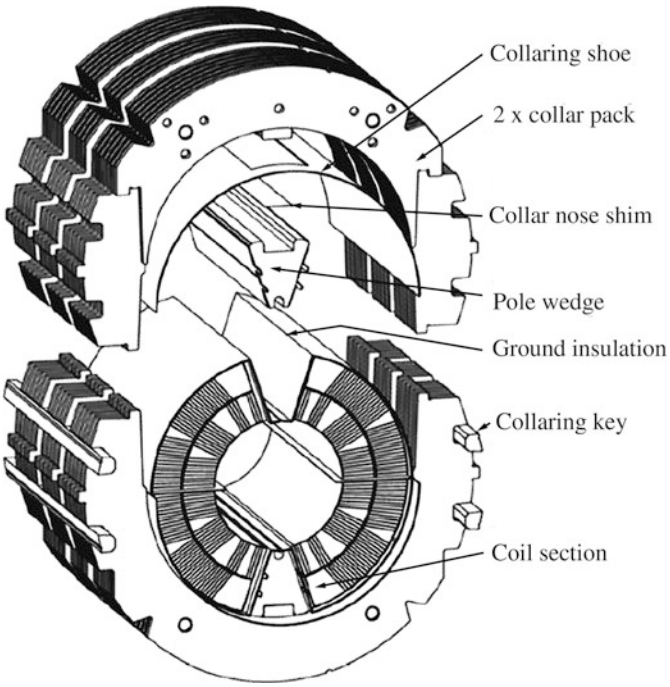

Fig. 9.8 Collared coil assembly

304 L stainless-steel strips are laminated onto the polyimide film with a 0.015 mm thickness of epoxy adhesive. A 0.005–0.015 mm thick Cu layer is coated between the heating stations to lower the total electrical resistance of the heater strips. The quench heaters for coils 101–109 and 111–113 were assembled with the coils after they had been impregnated; whereas those for coils 110 and 114–123 were impregnated with the coils to minimize the thermal resistance between them and the coil, and thus improve their efficiency. Recently, during standard re-commissioning electrical tests (test voltage 2.1 kV), a breakdown in the insulation system occurred. Based on this test result, it was decided to assemble the quench heaters with the coils after they had been impregnated, as previously done.

9.3.1.5 Collared Coil

The collared coil assembly is shown in Fig. 9.8. A rigid clamping and minimum coil distortion is attained with collars made of YUS130S austenitic steel (X8CrMnNiN 19-11-6 grade), pole wedges made of Ti-6Al-4 V titanium alloy, and a loading plate made of AISI 316 L stainless steel, covering the two layers on each side of the removable pole. Shims are placed between the pole wedges and the loading plate, and their size can be altered to regulate the azimuthal coil pre-stress, as needed. Extra shimming is also possible between the pole wedge and the collar nose.

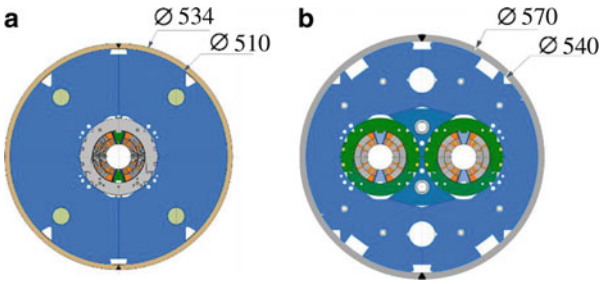

Fig. 9.9 CERN 11 T dipole cross-sections: (**a**) single-aperture; and (**b**) two-in-one-aperture. Dimensions in mm

The collaring procedure delivers a substantial part of the coil pre-stress. The collars are alternately assembled with their cavities upwards and downwards, and clamped around the coils in a press applying a force in the range 16–32 MN/m during collaring. To avoid coil damage during collaring, mechanical stops are used between the top and bottom collaring fixtures. To insert the collaring keys, the collars and the mechanical stops have to be pushed further by an extra 0.1 mm.

The stress in the coils during collaring should not exceed 150 MPa in the mid-plane, whereas it is substantially lower in the vicinity of the removable pole. Indirect control of the stress level in the coil is provided by strain gauges glued onto the noses of the collars. The use of the stresses measured in the collars in conjunction with the finite element model (FEM) allows the determination of the stresses created in the coil during collaring.

9.3.1.6 Short Dipole Models

The single- and two-in-one-aperture structures developed at CERN for the 11 T dipole (Savary et al. 2017) are shown in Fig. 9.9.

Single-Aperture Models

The collared coils are assembled with the half-yokes, the end plates, and the stainless-steel shells. The half-yokes have a vertically tapered gap with a resulting opening of 0.1 mm on the outer diameter, which is closed during shell welding and remains closed up to 12 T. A nominal 0.4 mm collar–yoke shim in the region of the collaring keys ensures the rigidity of the assembly, when most of the pre-stress is given by the collars in the single-aperture assembly. The axial forces, of the order of about 215 kN per pole, are taken up by the 55 mm thick end plates and by the shell, both made of 316LN stainless steel.

For MBHSP101 and the other models, the welding process consisted of a double root pass made with the tungsten inert gas (TIG) procedure. The end plates were then welded to the shell, and the bullet gauges (two per pole at each end) tightened with a torque of 25 Nm, corresponding to an axial pre-load of 8–9 kN per bullet.

Two-In-One-Aperture Dipole

The yoke of the two-in-one-aperture dipole is made of three parts. The central block, featuring a tapered surface at the interface with the yoke halves, is used for assembly purposes, and for locking the collared coils in the structure symmetrically during the assembly and welding of the skin. To tolerate the higher stresses in the two-in-one-aperture structure, the skin thickness was increased from 12 mm to 15 mm and the number of welding passes was increased.

9.3.2 Magnet Test

The main parameters and model tests in single- and two-in-one-aperture dipole configurations are summarized in Table 9.6.

9.3.3 Quench Performance

9.3.3.1 Model Magnet Limits

The maximum current reached in single-aperture model coils varies from 11.9–13.5 kA at 1.9 K, see also Table 9.6 (Willering et al. 2017, 2018). The maximum I/I_{ss} reached was 94% in the two-in-one-aperture coil DP101.

Two coils, SP102 and SP104, were limited at the layer jump at 1.9 K with 10 A/s ramp rate, while the other coils that were run to their limit were all limited in the mid-plane turn, see Fig. 9.10. Tests at 4.5 K confirmed the coil limits in mid-plane and layer jump, and in conductor block 3 of the inner layer. V–I measurements in DP102 show that all four coils have a reduction in I_c and n-value in the mid-plane inner layer turn (not localized, rather, distributed over a large fraction of it). Model

Table 9.6 Maximum current, short sample limit, and holding current tests for each model

Model	Coils	I_{max} (kA)	I_{ss} (1.9 K/4.3 K) (kA)
SP101	106, 107	11.9	14.5/13.1
SP102	106, 108	12.8[a]	14.5/13.1
SP103	109, 111	12.8[a]	14.2/12.8
DP101	106, 108, 109, 111	13.3	14.2/12.8
SP104	112, 113	12.3	14.4/13.0
SP105	114, 115	12.4	14.6/13.3
DP102	109, 112, 114, 115	11.4	14.4/13.0
SP106	116, 117	13.47	14.8/13.6
SP107	120, 121	12.85[a]	14.4/13.1

The nominal operating current is 11.85 kA, while 12.8 kA is the ultimate current
[a]Test target: no attempts to train higher

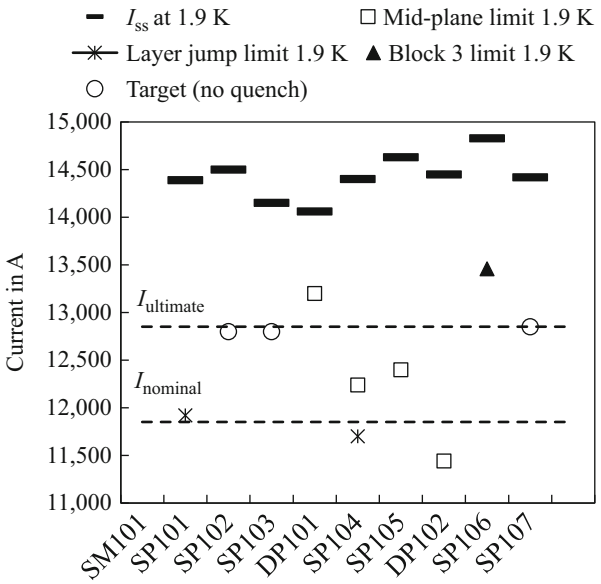

Fig. 9.10 Short sample limits and training limits at 1.9 K for the single-aperture and two-on-one-aperture models

magnets DP101 (coils 109 and 111), SP104, and SP105 also had mid-plane inner layer turn limitations. V–I measurements were not performed, however, and, especially for DP101, the limitation was at a much higher current. DP102 was recombined from coils that had previously been tested, but it was limited at a much lower current, showing that the conductor had been damaged during one of the production steps between the dismantling of the single-aperture model and the recombination into a two-in-one-aperture model. With the data available for these models it was suspected that the mid-plane suffered from irreversible degradation due to high levels of stress during the magnet's production. This behavior might also have been present in the first magnets; it was, however was only clearly detected from assembled coil 109–111 in DP101. From then it was clearly visible in all magnet assemblies. An extensive study was performed to investigate the maximum local stress level in the coils during all of the magnet construction steps, like collaring and yoking, and the damage levels due to stress on the cables, see Sect. 9.3.4 below. Meanwhile, SP106 was tested, showing a strongly reduced I_c and n-value, localized this time in the inner layer coil block 3 of coil 116. After magnet training, however, it reached a very high current value, see the following section.

9.3.3.2 Model Magnet Training

The single-aperture magnets were trained at nominal conditions at 1.9 K with a ramp rate of 10 A/s. Some of the models included coils that were already trained in a previous assembly. The training curves are shown as training per virgin coil, see Fig. 9.11.

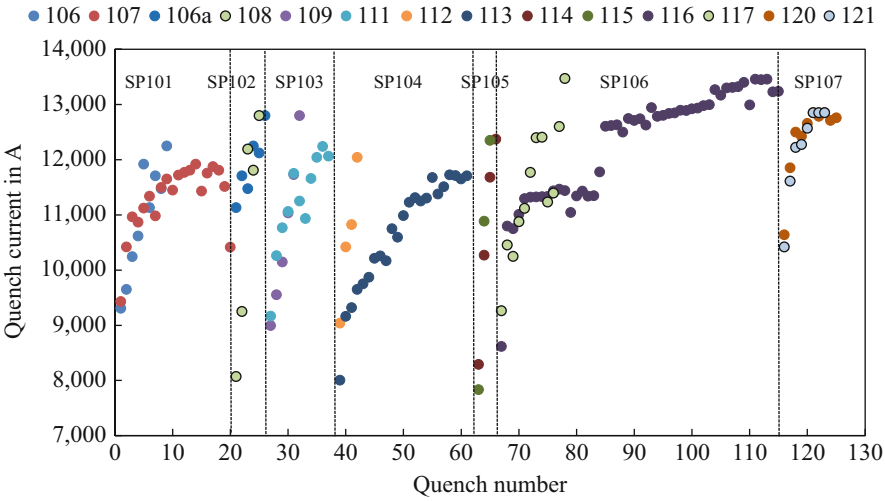

Fig. 9.11 Training quenches for all coils tested

In particular, the coils with layer jump issues, coils 107 and 113, show slow training. An excessive number of quenches are located in the pole turn and layer jump. These coils also show a low quench current limit in the layer jump region and, in addition, there is a strong suspicion of a local non-homogeneous defect in or close to the layer jump, which may have influenced the training rate (Willering et al. 2017). The particularly slow training of coil 116 may be linked with the I_c reduction in coil block 3 of the inner layer. Following quench 19, as shown in Fig. 9.11, the high MIITs (1 MIIT = 10^6 A^2 s) studies (part of the regular test program) started and the protection was delayed to increase the hot-spot temperature after a quench. While conductor degradation driven by the hot-spot was expected, the performance increased step by step, possibly due to a change of stress distribution in the conductor. This magnet went to 13.5 kA, with a central field of nearly 13 T.

Finally, note the significantly better behavior of coils 120 and 121, assembled in the single-aperture model SP107. They are based on the modifications introduced by the Task Force, see Sect. 9.3.4 below.

9.3.3.3 Training after Thermal Cycle

The number of retraining quenches needed to reach the same current as before the thermal cycle are shown in Table 9.7. In some cases there was only a thermal cycle, in other cases the collared coils were reassembled in a new yoke, while in others the coils were recombined and re-collared. In DP102 the coil limit (after conductor degradation during recombining of the coils) was reached without quench, but since it was at a much lower current it is left out of Table 9.7. In general, retraining after a thermal cycle is very fast, and the memory of the coils is very good. In particular, a

Table 9.7 Number of quenches needed to reach the same current as before the thermal cycle

Coil	Action performed during thermal cycle	Magnet	I_{max} (kA)	Number of quenches after thermal cycle
106	Re-collared	SP101 → SP102	11.8	3
106	Thermal cycle	SP102	12.5	2
106	Re-yoked	SP102 → DP101	12.8	2
108	Thermal cycle	SP102	12.5	0
108	Re-yoked	SP102 → DP101	12.8	0
109	Re-yoked	SP103 → DP101	12.8	0
111	Re-yoked	SP103 → DP101	12.8	0
116	Thermal cycle	SP106	13.0	0
117	Thermal cycle	SP106	13.0	0
120	Thermal cycle	SP107	12.85	2
121	Thermal cycle	SP107	12.85	0

good memory after re-yoking the collared coils is important. Coil 107 data for SP101 is not shown, since it already suffered strongly from erratic quenches before the thermal cycle, and is to be assumed irrelevant for memory after a thermal cycle.

9.3.3.4 Erratic Quenches

In model SP102 multiple erratic quenches occurred between 12–12.8 kA, with the quench origin mainly around the pole turn in the heads of the magnet and also around the layer jump. It is therefore remarkable that the same collared coil reached 13.3 kA while being part of two-in-one-aperture DP101, without showing the same behavior. It is generally thought that this behavior can be attributed to the increased and more uniform pre-stress and loading forces in the two-in-one-aperture dipole model compared to single-aperture models. Coils 107 and 113, having layer jump issues, showed erratic quench behavior.

9.3.3.5 Detraining/Degradation During Power

Of all the coils, only coil 107 in model SP102 had detraining or degradation observed during powering. The quenches occurred in the layer jump, a part of the coil for which a non-homogeneous degradation had already been identified. This area is mechanically sensitive due to the discontinuity between the two layers, however no direct evidence of the cause of detraining/degradation was found during cold tests or after coil cutting after the test.

9.3.3.6 Holding Current Tests

A holding current test was performed for all models, either at the ultimate current level of 12.8 kA, or at a current just below the training limit of the magnets. The duration varied between 1 h and 10 h, depending on the time available for the test (Willering et al. 2017, 2018). It should be noticed that, except for MBHSP104, which quenched after 1 h 5 min in the known defective layer jump of coil 113, the magnets showed stable behavior.

9.3.3.7 Temperature Dependence

In Fig. 9.12 the maximum currents reached at 1.9 K and 4.5 K are compared for six of the models. The expected reduction in quench current is 5–15%, in line with the expected 10% due to I_c reduction from 1.9 K to 4.5 K. SP106 has relatively lower performance at 4.5 K, and SP101 has relatively better performance at 4.5 K.

9.3.3.8 Ramp Rate Dependence

For some models, ramp rate studies have been critical to assess that limitations were not due to mechanical causes (like movements). This showed that quench limits were mainly due to the conductor, mainly in the mid-plane or pole turn. In SP104 the highest quench current was reached at an elevated ramp rate of 50 A/s, pointing at non-homogeneous degradation in the pole turn. The results of ramp rate studies of SP106 and SP107 are shown in Fig. 9.13. The measurements at 1.9 K and 4.5 K give consistent results for I/I_c for both magnets. The slope for both coils is similar, but

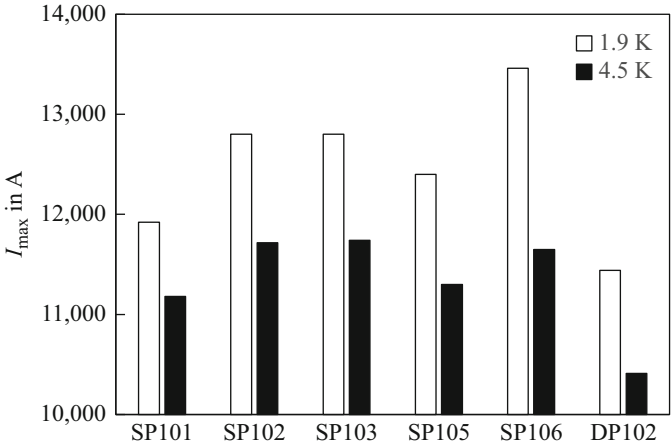

Fig. 9.12 Quench performance comparison between 1.9 K and 4.5 K temperatures for six magnets

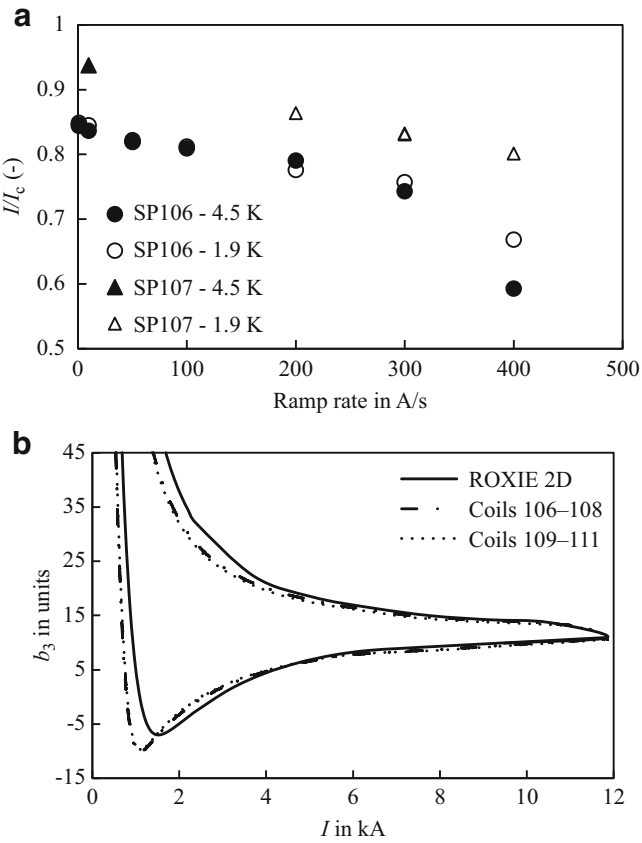

Fig. 9.13 (**a**) Ramp rate quench dependence for SP106 and SP107 models (the latter is the high performance model following the Task Force design revision, see Sect. 9.3.4 below). The current is normalized to the short sample limit. (**b**) Measured and calculated b_3 vs. current for DP101

with SP106 reaches a lower current level throughout. In SP106 most quenches occurred in block 3, while in SP107 the quenches started in the mid-plane turn.

9.3.3.9 Splices

All Nb_3Sn to Nb-Ti splices that have been measured had a resistance between 0.1 and 0.3 nΩ (Willering et al. 2018), which is a very good level according to the design. No quenches or anomalies were found around the splices in all models of magnets.

9.3.3.10 Magnetic Measurements

Comprehensive magnetic measurements were carried out to determine the MBH transfer function (TF) and the field harmonics produced by the coil geometry, persistent currents, iron saturation, and magnetic cross-talk between apertures (Fiscarelli et al. 2016, 2017). The measurements were performed using the CERN Fast Measurement Equipment (FAME) system. It is suitable for tests in a horizontal position at ambient temperature as well as for a vertical cryostat at helium temperature. Field harmonic coefficients are presented at the reference radius $R_{\text{ref}} = 17$ mm.

The magnet TF was measured at 1.9 K by powering the magnet with a stair-step cycle. Measured geometrical and saturation components agree well with the 2D data calculated using the Routine for the Optimization of magnet X-sections, Inverse field calculation and coil End design (ROXIE) at currents above 2 kA. At low currents the persistent current effect is visible, as expected.

Figure 9.13b shows the measured and calculated b_3 vs. the magnet current for both apertures. Measurements and calculations agree well for both apertures. Below 2 kA, the measured persistent current effect in b_3 diverges from calculations. A similar discrepancy was also observed in the 11 T dipole models tested at FNAL. Although the persistent current effect in b_3 is large, the b_3 variation between injection and nominal field is about 22 units, within the acceptable level of 27 units. It should be noted that calculations are performed with a model that limits the magnetic moment of the wires at low field, in the region where the magnetization collapses due to flux jumps. This choice reduces considerably the effect of persistent currents at low field (Izquierdo Bermudez et al. 2016).

The saturation of the iron separating the two apertures results in magnetic cross-talk, with effects mostly visible for b_2 harmonics, see Fig. 9.14. The compensation is not perfect; it is, however, good enough to be acceptable for operation.

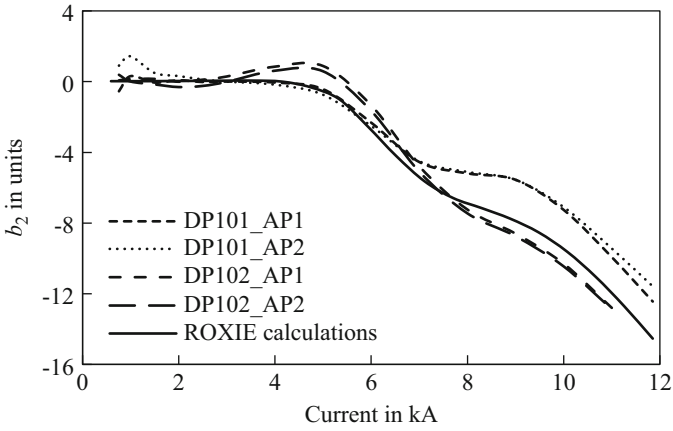

Fig. 9.14 Measured b_2 harmonic over the whole dynamic range for DP101 and DP102, compared with calculation. (Courtesy of L. Fiscarelli, CERN)

Table 9.8 Field harmonics at $I = 3.5$ kA for DP101

	2D calculations		Coils 106, 108		Coils 109, 111	
n	b_n	a_n	b_n	a_n	b_n	a_n
2	−0.07	0.00	−1.80	4.17	−0.09	6.30
3	7.46	0.00	11.85	−1.12	11.54	0.13
4	0.00	0.00	−0.31	0.15	−0.65	0.99
5	−0.01	0.00	1.25	−0.01	1.58	−0.65
6	0.00	0.00	−0.13	−0.11	−0.17	0.31
7	−0.09	0.00	0.15	−0.11	0.21	−0.18
8	0.00	0.00	−0.04	0.04	−0.05	0.02
9	0.91	0.00	0.65	0.06	0.70	−0.31

The ramp-rate effect on normal and skew multipoles was measured in current cycles with ramp rates of 40 and 80 A/s. As expected, and similar to the FNAL models, the effect is small due to the use of a cored cable.

At 1.9 K, the geometrical harmonics were defined as the average measured values on the current up and down ramp branches of the stair-step cycle at the magnet current of 5 kA. Table 9.8 presents the measured harmonics in the central section of the two apertures of DP101 and the calculated values for the nominal 2D coil geometry. The main differences are in a_2 and b_3, which can be explained by errors in the coil's actual position and coil deformations during magnet assembly, and should be corrected with a more rigorous procedure for the long magnets. A very recent measurement on the first prototype confirms this expectation.

9.3.4 Design Revisions by the 11 T Task Force

Following the test of single-aperture models SP104 and SP105, and the test of the same coils in the two-in-one-aperture configuration DP102, it became increasingly clear that the conductor performance in the CERN models was well below the expected level. As anticipated in the discussion of the powering test results, training reached a plateau at high field, at which point quenches appeared to be reproducible, with no precursors, an identical location, and a very similar voltage "signature." A good example of this behavior is the plateau reached after the eighth training quench in the single-aperture model SP105, followed by a sequence of seven identical quenches (one de-training during the sequence).

The reasons for this performance limitation became clear by taking direct high-resolution measurements of the voltage-current characteristics of the limiting coil, in the portion where the quench origin was identified. One such measurement is reported in Fig. 9.15, taken in the worst 1.3 m long straight cable segment in the limiting coil 109 of two-in-one-aperture model DP102. We see that there is a clear voltage rise as the current is ramped, well in advance of the quench, and well below the projected critical current at the field and temperature operating conditions. Based on the early onset, the magnitude of the measured voltage, its reproducibility, and

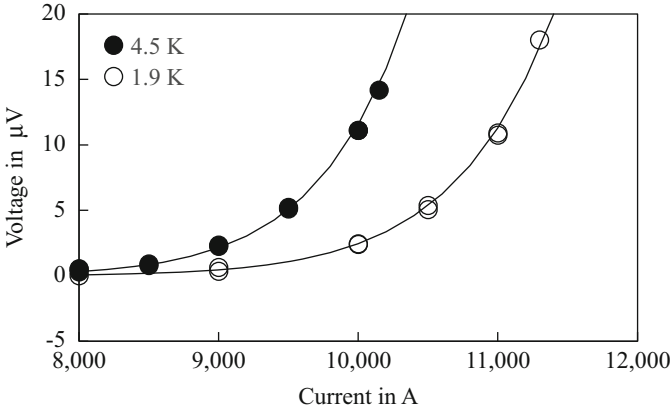

Fig. 9.15 Voltage–current characteristics in model DP102 (mid-plane segment 109 II-I1), for the worst coil

stable magnet behavior under the quench current, we have attributed this early V–I appearance to extensive irreversible degradation of the conductor in the mid-plane of the coil. In fact, measurements of voltage during ramping in all coils of two-in-one-aperture model DP102 have shown that this is not a feature of a single coil location but, rather, a systematic behavior.

The voltage in the other coils is, however, not sufficient to yield to a quench, and can be sustained in stable conditions. The final crucial information is that repeated cycling to high current, as well as repeated quenching, did not cause an observable change in this behavior, indicating that the irreversible degradation is not associated with electromagnetic loads, but must have occurred during manufacturing or cool-down. This observation was complemented by the independent finding that the C-shaped mica sheet wrapped around the cable, with a gap of approximately 7 mm in the middle, is a potential stress intensifier at the cable edges, which has been verified in several instances. An example is shown in Fig. 9.16, where we report the pressure measurement film (PMF) imprints (Fuji prescale film) obtained from a measurement of the mid-plane stress during a pre-collaring operation taken in single-aperture model SP105 at full load (key insertion), corresponding to a target average stress of 120 MPa. As shown, the local stress in the cable edges can be much higher than the average pressure exerted on the whole cable surface, with a distribution that has a range at least as wide as 120 MPa. The actual range may be even larger, but it is difficult to make an accurate assessment because of saturation of the pressure measurement film. The stress peaks are in correspondence with the wrapped edge of the mica foil, and a reduction of stress is observed in the center of the cable where the mica foil wrap has a gap.

The above findings triggered an analysis of coil production and assembly, with the aim of finding the step where the irreversible degradation took place. Measurement of stress in the collar nose, PMF imprints taken during simulated collaring

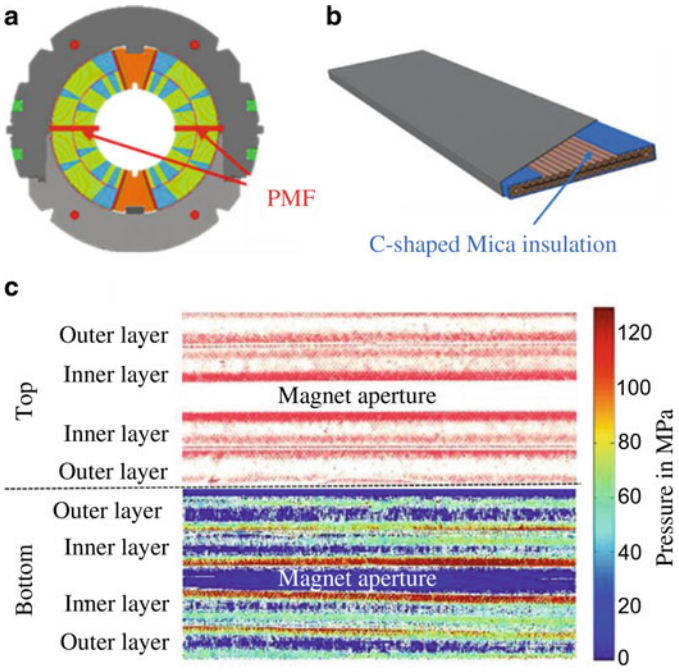

Fig. 9.16 (**a**, **b**) Schematic of the original insulation scheme with incomplete "C" wrap (blue); and (**c**) pressure measurement film (PMF) imprints obtained during collaring tests in single-aperture model SP105. The PMF results have been scanned and translated to values of pressure in MPa. (Courtesy of S. Izquierdo Bermudez and F. Wolf (CERN))

steps, and FEM analysis, point to the collaring step and, in particular, under the press at the insertion of the keys, as the most stressed situation for the coil mid-plane. In particular, combining the direct stress measurements during collaring of the magnet models and the expected stress intensification associated with the mica wrap explained above, it is expected that the local stress exerted on the thin cable edge of the mid-plane of the coils in model magnets SP104 and SP105 (and DP102) reached values well above the 150 MPa target, which at the time was the limit set to avoid irreversible conductor degradation.

A final element in this analysis is the actual conductor insulation thickness. The original insulation system of the 11 T cable consists of a partial wrap with a mica foil of 80 μm thickness and 25 mm width, and 11 tex S2-glass fiber braided on top. The nominal thickness, defined under a pressure of 30 MPa, was taken as 100 μm during the coil design phase. In practice, the thickness obtained in production was quite different from the nominal value. Specifically, the measured insulation thickness was found to be in the range 117 μm (at 30 MPa) to 135 μm (at 5 MPa). This additional thickness accumulates in the coil, resulting in a denser and stiffer coil, which can exacerbate the stress peaking effect described above.

Based on the observations above, some of the design aspects were reconsidered and an iterative process was started, consisting mainly of the following.

Review and Modification of the Insulation Scheme The modifications made to the insulation system consisted firstly in a more complete coverage of the cable perimeter, using a wider mica foil. A nominal width of the mica foil of 31 mm results in a gap reduction from the original 6.9 mm to 0.9 mm. In addition, the number of picks per cm of the glass fibers was increased (from seven to nine) with a reduction of the number of plies per strand (from nine to four). This change to the braiding yields a reduction of the nominal thickness of insulation to the desired 100 μm, measured under a transverse pressure of 5 MPa, i.e., leaving sufficient room for the dimensional changes to the conductor during heat treatment.

Characterization of the Transverse Stress Limit of Insulated Cables The main aim was to determine quantitatively the degradation limits of the 11 T Nb_3Sn cable in its final configuration (strand, cable, and insulation system). The quantity sought is the pressure at which the insulated cable is irreversibly degraded, most likely due to the development of cracks in the filaments. This limit is a critical input for the determination of a safe collaring procedure. The results collected to date point to a critical stress of 175 MPa as the maximum allowable local value, beyond which the conductor is irreversibly degraded. Extensive studies, including micrographs, have shown that beyond this stress the filaments start cracking. These findings confirm the limit applied for the collaring, i.e., 150 MPa peak stress at any location.

Testing of the Mechanical Properties of the 11 T Winding The nominal dimensions of the coil cavity defined by the collars must be adapted by acting on the pole, mid-plane, and radial shims to induce mechanical interference, and thus produce the required azimuthal and radial pre-stress. Accurate knowledge of the stiffness of the coil in relation to the applied stress and coil deformation is hence a critical input for the selection of these shims. In fact, the coil stiffness for an Nb_3Sn epoxy impregnated coil of 20–40 GPa is typically a factor of three to four higher than that for a Nb-Ti polyimide insulated coil in the range 8–15 GPa. Tolerances in the assembly, and uncertainties in the coil dimensions and stiffness, translate therefore into a much greater variation of pre-stress than is customary in Nb-Ti, which, in combination with a hard limit on the maximum allowable stress described above, makes the collaring step a balancing act. For these reasons we have performed extensive mechanical measurements of impregnated stacks of cables and cut-out portions of windings.

The relationship between stress and deformation is highly non-linear, exhibiting significant hysteresis and ratcheting. The equivalent modulus in virgin loading conditions derived from the above measurements is around 10–20 GPa, while further loading gives values in the range 25–35 GPa. This value is to be compared to measurements on cable stacks, which in comparable conditions give a virgin modulus of 15 GPa and successive loading values of 40 GPa. It is clear from these results that a single value for coil stiffness is not an appropriate parameter: rather, the complete behavior of loading and unloading must be taken into account when

analyzing the stress and strain state of the coil under the various manufacturing and loading steps. Still, the mechanical properties are affected by a large uncertainty, typically 30% of the equivalent coil stiffness. Given this complexity, the initial working assumption was to use FEM to select the appropriate shim size, on a case-by-case basis. The burden of such analyses, and the inherent uncertainty in the value of the mechanical characteristics, has, however, motivated a different approach to coil shimming, as described below.

Experimental Analysis of the Collaring The last major element of R&D was the experimental analysis of the collaring procedure, with the aim of establishing a direct correlation between the coil–collar interference and the resulting pre-stress. A number of collaring trials were performed using short segments cut out of representative production coils and highly instrumented collar packs. Pressure measurement systems were used for additional diagnostics in the collared coil assembly to supply a direct measurement of the stress at the coil mid-plane and at the collar–pole interface. Among the systems considered, scanned and processed PMF imprints were the most practical and effective. Several tests were performed on different coils, changing the azimuthal shims so as to modify the coil–collar interference. We define the coil size *excess* as the sum of the interference of the right and left coil halves, taking into account that each different coil segment may have different dimensions. The results are very interesting in that they show that, to limit the maximum mid-plane stress to less than 150 MPa, the coil size excess must be kept below 300 μm, which provides a very simple recipe for the collaring operation. Note that with this choice of interference, and given the specific collaring mechanics and collar dimensions (influencing spring-back), the residual stress at the pole is around 50 MPa. This stress is in principle not sufficient to maintain contact at full powering.

The changes above were implemented as part of a fast-track effort in two single-aperture short models, MBHSP107 and MBHSP108, for which a total of six coils were built, coil 118 to coil 123, before the construction of the first long magnet for the HL-LHC. Care was taken that the short coils were all built with final components, and, in particular, strand, cable, and insulation. Also, the models were produced using as much as possible the same methods and procedures applied to the construction of the long magnets, so as to provide early and valuable feedback.

To date, the results for single-aperture model MBHSP107, achieving ultimate performance with the fastest training among all short models, and showing no limitations within the operating range, have confirmed the soundness of the modifications introduced. While definitive conclusions can only be drawn after the testing of SP108, in order to verify the reproducibility of these results, the design changes described in this section were introduced into the series production magnets (it was too late for their introduction in the prototype).

This result also indicates that the pre-load required for operation at high field may not be as high as the computed average electromagnetic load, which has relevance both for the 11 T dipole as well as for R&D for higher fields.

9.3.5 *Full-Scale Prototype*

A full-length prototype has been fabricated at CERN (Savary et al. 2018). This prototype has all the features of the final magnets, except for the modifications introduced by the Task Force's revised design and procedures, see above. It has been a key learning and debugging exercise for such a complex object: indeed, this 5.5 m long dipole is the first long Nb_3Sn magnet built at CERN, and the longest Nb_3Sn accelerator magnet built so far. Besides the importance of the 11 T dipole itself, we consider it a strategic step paving the way for the 7.2 m long coils of MQXF, the inner triplet quadrupole for HL-LHC. The prototype is targeting full accelerator quality in terms of quench performance, field errors, electrical robustness, protection, and geometry. Although most of the major tooling was available at CERN, recovered from the production of the Nb-Ti magnets for the LHC, significant modifications and upgrades were necessary. The largest additional tooling required to fabricate the coils were an argon oven for the reaction of the Nb_3Sn conductor, and a vacuum pressure impregnation system. The design and procurement of the contact tooling started in the middle of 2013 with the winding mandrel and curing mold, followed by the reaction fixture and impregnation mold, to finish later with the collaring tooling. Because of a tight schedule resulting from the need to install the magnets during the accelerator's LS2 during the years 2019–2020, an important overlap between the different phases of the project was inevitable. The assembly work profited from the large amount of experience in the assembling and collaring of long coils and the assembly of long cold masses at CERN for the LHC magnets.

To optimize the overall duration of development and production activities, it was decided to involve industry from the beginning of the prototyping activities at CERN. Contracts were placed with four companies, namely Alstom Power Systems in France, ASG Superconductors in Italy, BNG in Germany, and Oxford Instruments in the UK. These companies contributed to the design of the tooling, the construction activities, and to a certain extent also to the analysis of the magnet models' performance. To our knowledge, it is the first time that European Union (EU) industry was asked to contribute at this stage of an accelerator magnet project. This also allowed technology transfer to be carried out *in the shadow* of the development activities, and the anticipation of the industrialization of magnet production.

Three practice coils were made, one with copper conductor and two with low-grade (meaning not fully qualified) superconducting wire, to develop the procedures, train the technical staff, and commission the machines and tooling. Five full performance coils were then fabricated: one was lost in an incident and four have been assembled in the prototype. Special attention was required for the fabrication of the long coils, especially for the reaction and impregnation processes, which are specific to Nb_3Sn. Dealing with the thermal contraction of such long coils, however, proved to be more difficult than expected, and large gaps appeared after reaction, especially in the heads region. Although the gaps were filled with glass fiber this is

Fig. 9.17 The first 5.5 m long 11 T MBH dipole prototype in its cryostat at CERN ready to be transported to the test bench

most likely to be a weak point in the fabrication. The revised design suggested by the Task Force, discussed above, is supposed to address this issue.

The two practice coils (CR01 and CR02), made of low-grade wire, were assembled with the collars to validate the collaring process and tooling. The first collared coil assembly for the prototype was made with coils CR04 and CR05, and the second collared coil assembly with coils CR06 and CR07.

The prototype with its cryostat was finished in May 2018, see Fig. 9.17, and swiftly tested. The first test campaign showed that coil CR07 was damaged at both ends, limiting the performance to a value below nominal of 10 kA. Damage to one coil is suggested by the fact that both ends of that coil have a quench current limit well below the nominal value. The same coil shows resistive behavior (4.5 nΩ) at low current. Although at present the exact nature and location of the damage are not clear, production records show that the ends of coil CR07 had large gaps after heat treatment, nearly 10 mm that needed to be filled and required some manipulation at the level of the pole and end spacers. Ramp rate studies showed typical "inverse" behavior, i.e., higher quench values at higher ramp rates, which is a sign of an issue with the conductor (either localized or distributed, it is difficult to disentangle). Investigations about a possible correlation and cause are ongoing, especially trying to understand whether there is any scale-up effect, from the models to the long prototype coils. The fact that the first long prototype contains at least one coil that is damaged shows the importance of the adjustments devised by the Task Force in order to have more uniform and predictable results.

9.3.6 Series Production

Series production of the 11 T models comprises four magnets for installation in the LHC machine, and two spare magnets. For this, 12 collared coils are to be produced; the plan foresees the production of 30 single coils, of which six coils may be used to cover for possible incidents during production. The design and construction procedures integrate all recommendations issued by the Task Force.

In order to cope with the tight schedule requirements, following competitive tendering a service contract was placed with Alstom Power Services, Belfort, France, now part of General Electric. The work is to be carried out at CERN in the Large Magnet Facility, where all of the necessary machines and tooling are available from the prototyping phase. All of the components and consumables are to be provided by CERN. Some of the tooling has been duplicated in order to allow the achievement of the scheduling requirements. The contract comprises a start-up phase during which the personnel of the contractor can learn the manufacturing and inspection procedures that have been made available by CERN. The total duration of the contract will be of the order of 30 months. The other construction activities, like the cold mass assembly, the cryostating, the cold tests, and the final preparation prior to installation in the accelerator, will be carried out by a mixed team of CERN personnel and contract labor under direct CERN technical responsibility.

9.4 Conclusions

The 11 T dipole project for the HL-LHC is very demanding from both the technical and scheduling points of view. The initial technology transfer from FNAL to CERN, especially in cable design and coil technology, has been very important to curb the work and meet the schedule. The design contains both some revisited as well as novel features, e.g., the insulation system and other coil components, featuring a new original removable pole collaring concept. A total of 23 coils (including practice coils of copper or low-grade superconductor cables), all 2 m long, have been manufactured to date, and most of them have been assembled in seven magnet models with single apertures at CERN. Two two-in-one-aperture dipole short models were also assembled and tested. Models MBHSP102, MBHSP103, and MBHDP101 have shown satisfactory training performance and memory, and acceptable field quality, compatible with the installation requirements for the LHC machine. Models SP101, SP104, and SP105 showed limitations that were usually understood and traced to damage to the layer jump region or to the conductor due to excessive local pre-stress in the mid-plane. One magnet with slow training behavior, SP106, was pushed to a very high current quench value by gradually increasing the hot-spot temperature (delaying protection). The second two-in-one-aperture assembly, DP102, was limited to below the ultimate current due to damage to all of the coils that were good in the single aperture test. Altogether, these results indicated

that the conductor and the coil design are adequate to reach the ultimate current, however the design with the assembly procedures used in the model R&D phase is very vulnerable to damage due to an excess of pre-stress, especially in the mid-plane.

The very good results, especially in terms of memory (always very good), have justified proceeding towards long magnets. The issue of a possible excess of stress was thoroughly investigated by a Task Force and a few changes in the design and in the collaring procedure were introduced and validated with SP107, which showed the best quench behavior among all models (very few quenches to ultimate current and almost perfect memory after a thermal cycle). While the prototype has been essential to debug all of the chain of construction for long magnets, only the first series dipoles will contain all elements of the basic and revised design, and we are very confident that we can meet the HL-LHC objective of installing the successful 11 T long cryo-assembly dipole in 2020, the first magnets wound with Nb_3Sn to operate in an accelerator.

The operation in a very demanding and precise collider like the LHC should show definitively the suitability of high field magnet technology for proton colliders, probably the most demanding application of superconductivity at present.

References

Ahlbäck J, Ikäheimo J, Järvi J et al (1994) Electromagnetic and mechanical design of a 56 mm aperture model dipole for the LHC. IEEE Trans Magn 30(4):1746–1749. https://doi.org/10.1109/20.305594

Andreev N, Barzi E, Chichili DR et al (2002) Volume expansion of Nb-Sn strands and cables during heat treatment. Adv Cryog Eng 48(614):941. https://doi.org/10.1063/1.1472635

Apollinari G, Béjar Alonso I, Brüning O et al (eds) (2017) High luminosity large hadron collider (HL-LHC): technical design report V.0.1, CERN-2017-007-M. CERN, Geneva

Auchmann B, Karppinen M, Kashikhin VV et al (2012) Magnetic analysis of a single-aperture 11 T Nb_3Sn demonstrator dipole for LHC upgrades. In: Proceedings of IPAC2012: international particle accelerator conference, New Orleans, May 2012, p 3596

Bottura L, de Rijk G, Rossi L et al (2012) Advanced accelerator magnets for upgrading the LHC. IEEE Trans Appl Supercond 22(3):4002008. https://doi.org/10.1109/tasc.2012.2186109

Brüning O, Rossi L (eds) (2015) The high luminosity large hadron collider – the new machine for illuminating the mysteries of universe. Advanced series on direction in high energy physics, vol 24. World Scientific, Singapore. https://doi.org/10.1142/9581

Carli C (ed) (2010) Proceedings of the Chamonix 2010 workshop on LHC performance, Chamonix, 25–29 Jan 2010, CERN-ATS-2010-026. CERN, Geneva

Damerau H, Funken A, Garoby R et al (eds) (2014) LHC injectors upgrade—technical design report, vol 1, protons, CERN ACC.2014-0337, 15 Dec 2014. CERN, Geneva

de Rijk G, Milanese A, Todesco E (2010) 11 Tesla Nb_3Sn dipoles for phase II collimation in the Large Hadron Collider, sLHC Project Note 0019. CERN, Geneva

Fiscarelli L, Auchmann B, Izquierdo Bermudez S et al (2016) Magnetic measurements and analysis of the first 11-T Nb_3Sn dipole models developed at CERN for HL-LHC. IEEE Trans Appl Supercond 26(4):1–5. https://doi.org/10.1109/tasc.2016.2530743

Fiscarelli L, Izquierdo Bermudez S, Dunkel O et al (2017) Magnetic measurements and analysis of the first 11-T Nb_3Sn 2-in-1 model for HL-LHC. IEEE Trans Appl Supercond 27(4):1. https://doi.org/10.1109/tasc.2016.2639285

Holzer B (2014) Impact of Nb_3Sn dipoles on the LHC lattice and beam optics, CERN ACC-NOTE-2014-0063. CERN, Geneva

Izquierdo Bermudez S, Bottura L, Todesco E (2016) Persistent-current magnetization effects in high-field superconducting accelerator magnets. IEEE Trans Appl Supercond 26(4):1–5. https://doi.org/10.1109/tasc.2016.2519006

Karppinen M, Andreev N, Apollinari G et al (2012) Design of 11 T twin-aperture Nb_3Sn dipole demonstrator magnet for LHC upgrades. IEEE Trans Appl Supercond 22(3):4901504. https://doi.org/10.1109/tasc.2011.2177625

Rossi L (2004) Experience with LHC magnets from prototyping to large scale industrial production and integration. In: Proceedings of EPAC2004. 9th European particle accelerator conference, Lucerne, July 2004, LHC Project Report 730. CERN, Geneva, p 118

Savary F, Apollinari G, Auchmann B et al (2015) Design, assembly, and test of the CERN 2-m long 11 T dipole in single coil configuration. IEEE Trans Appl Supercond 25(3):1–5. https://doi.org/10.1109/tasc.2015.2395381

Savary F, Bajko M, Bordini B et al (2017) Progress on the development of the Nb_3Sn 11 T dipole for the high luminosity upgrade of LHC. IEEE Trans Appl Supercond 27(4):4003505. https://doi.org/10.1109/tasc.2017.2666142

Savary F, Bordini B, Fiscarelli L et al (2018) Design and construction of the full-length prototype of the 11-T dipole magnet for the high luminosity LHC project at CERN. IEEE Trans Appl Supercond 28(3):1–6. https://doi.org/10.1109/tasc.2018.2800713

Willering GP, Bajko M, Bajas H et al (2017) Cold powering performance of the first 2 m Nb_3Sn DS11T twin-aperture model magnet at CERN. IEEE Trans Appl Supercond 27(4):1–5. https://doi.org/10.1109/tasc.2016.2633421

Willering G, Bajko M, Bajas H et al (2018) Comparison of cold powering performance of 2-m-long Nb_3Sn 11 T model magnets. IEEE Trans Appl Supercond 28(3):1–5. https://doi.org/10.1109/tasc.2018.2804356

Zlobin AV (2010) Status of Nb_3Sn accelerator magnet R&D at Fermilab. In: 'EuCARD – HE-LHC'10. AccNet mini-workshop on a "high-energy LHC", Villa Bighi, 14–16 October 2010, CERN Yellow Report CERN-2011-003 (arXiv:1108.1869). CERN, Geneva, p 50

Zlobin AV, Andreev N, Apollinari G et al (2012) Design and fabrication of a single-aperture 11 T Nb_3Sn dipole model for LHC upgrades. IEEE Trans Appl Supercond 22(3):4001705. https://doi.org/10.1109/tasc.2011.2177619